Electronic Supplementary Material (ESI) for Journal of Materials Chemistry A.

Electronic Supplementary Information (ESI)

Spray-drying synthesis and vanadium-catalyzed graphitization of a nanocrystalline γ-$Li_{3.2}V_{0.8}Si_{0.2}O_4$/C anode material with a unique double capsule structure

Keisuke Matsumura[a], Etsuro Iwama[a,b,c,*], Kenta Takagi[a], Naoki Hashizume[a], Yu Chikaoka[ab], Naohisa Okita[a], Wako Naoi[d], and Katsuhiko Naoi[a,b,c,*]

[a] *Department of Applied Chemistry, Tokyo University of Agriculture & Technology, 2-24-16 Naka-cho, Koganei, Tokyo 184-8558, Japan*

[b] *Global Innovation Research Organization, Tokyo University of Agriculture & Technology, 2-24-16 Naka-cho, Koganei, Tokyo, 184-8588 Japan*

[c] *Advanced Capacitor Research Center, Tokyo University of Agriculture & Technology, 2-24-16 Naka-cho, Koganei, Tokyo 184-8558, Japan*

[d] *Division of Art and Innovative Technologies, K & W Inc., 1-3-16-901 Higashi, Kunitachi, Tokyo 186-0002, Japan*

* Corresponding Authors: iwama@cc.tuat.ac.jp (E. I.), k-naoi@cc.tuat.ac.jp (K. N.)

Changes in XRD and XAFS profiles during the synthesis process:

All the XRD patterns of γ-LVSiO/C at each step of the synthesis, including solid-state reaction (γ-LVSiO), ball-milling (pulverized γ-LVSiO), spray-dry and carbonization (γ-LVSiO/Carbon composite), were indexed to the space group *Pnma* of the of the γ-phase $Li_{3.6}V_{0.4}Si_{0.6}O_4$ (ICDD #56-1495) (Fig. 1). The full width at half maximum (FWHM) of the XRD peaks for each sample increased with progress in the synthetic step, indicating the reduction of the apparent average crystallite sizes of γ-LVSiO. The crystallite sizes of those samples were calculated from FWHMs of 200, 020 and 002 peaks by using the Scherrer equation (eq. S1), which are summarized in Table S1. The crystallite size after spray dry/carbonization was 30% smaller than that of the pulverized γ-LVSiO despite the carbonization process at 700°C possibly inducing particle growth. Such reduction in crystallite size indicates a partial dissolution of γ-LVSiO in the aqueous feed solution, which is analogue to previously reported "water-etching of LVO" [1, 2].

Table S1. The peak full width at half maximum of the XRD patterns for the γ-LVSiO samples at each step of the synthetic procedure (as shown in Fig. 1) with the corresponding crystallite size calculated by the Scherrer equation [3, 4] (eq. S1).

	FWHM/ deg			Crystallite size (Scherrer) / Å		
	200	020	002	200	020	002
γ-LVSiO	0.0713(8)	0.078(2)	0.0679(6)	1175(13)	1099(32)	1283(12)
Pulverized γ-LVSiO	0.096(3)	0.143(7)	0.116(3)	875(24)	599(28)	749(18)
γ-LVSiO/Carbon composite	0.136(6)	0.187(8)	0.155(13)	616(28)	458(19)	564(48)

$$B = \frac{K\lambda}{\beta \cos\theta} \quad \text{(eq. S1)}$$

In the equation, B is the mean size of the crystallite domains, β is the FWHM, θ is the Bragg angle, λ is the X-ray wavelength, K is the Scherrer constant where K=0.9.

For detail investigation of the crystal structures, X-ray absorption fine structure (XAFS) spectra for the γ-LVSiO samples at each step of the synthetic procedure were measured in transmission mode at the beamline BL01B1 of the synchrotron radiation facility Spring-8 (Hyogo, Japan). As shown in Fig. S1a, V-K edge XANES spectra for three samples are well overlapped, indicating that local fine structure surrounding vanadium was not changed in progress of the synthetic process. Such XANES profiles with a sharp pre-edge peak at *ca.* 5460 eV correspond to the reported typical spectra of β-Li_3VO_4 crystals[5] with the energy position of absorption edge relatively consistent with the reference of V_2O_5 powder sample, meaning the oxidation state of V^{5+} in the γ-LVSiO samples. Furthermore, radial distribution function obtained from EXAFS signals for the γ-LVSiO samples (Fig. S1b) supports that above discussion that their local fine structure was not changed in the synthetic procedure. A single peak at 1.35 Å of the radial distance from vanadium indicates existence of the nearest-neighbor oxygen atom.

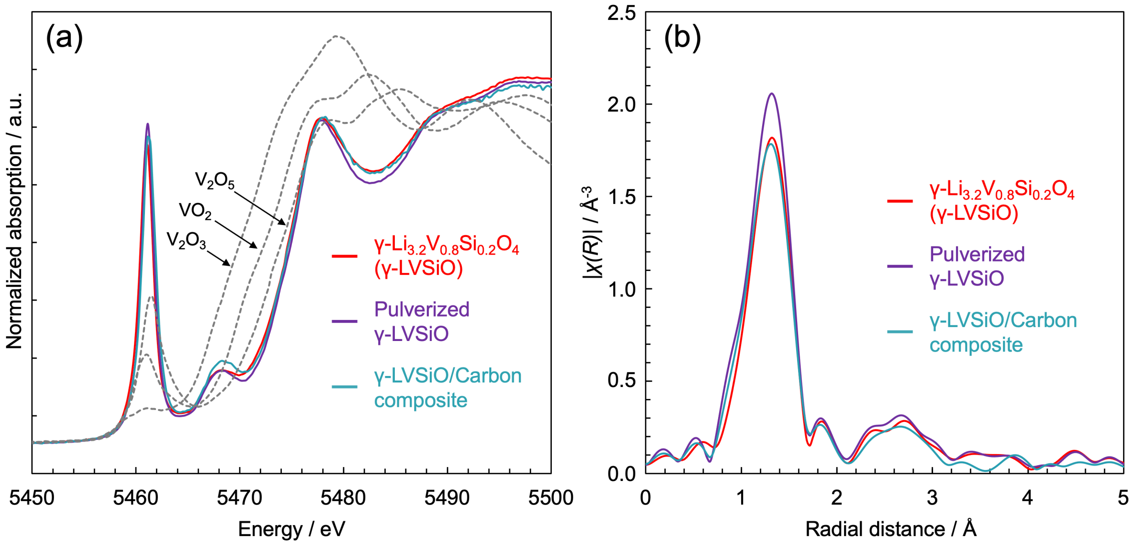

Fig. S1. (a) V-K edge XANES spectra for the γ-LVSiO powder samples at each step of the synthetic procedure (as shown in Fig. 1) along with the spectra for reference powder samples of V_2O_5 (V^{5+}), VO_2 (V^{4+}), and V_2O_3 (V^{3+}). These spectra for the γ-LVSiO are well overlapped with a sharp pre-edge peak at *ca.* 5460 eV. (b) Corresponding radial distribution functions obtained from Fourier transformation of the k^2-weighted EXAFS signals. Those of the three samples exhibited a single peak at same radial distance of *ca.* 1.35 Å.

Cross-sectional SEM image with EDS elemental maps for the γ-LVSiO/C capsule:

To confirm the detail morphology of the γ-LVSiO/C capsule, the cross-sectional SEM image (Fig. 2b) was observed with corresponding EDS elemental maps of C, V, Si, and O (Fig. S2). The C atoms as well as other atoms (V, Si, O) are uniformly distributed throughout the capsule, indicating a successful carbon compositing of the γ-LVSiO particles. Such well dispersed carbon may play a role as buffer to prevent a growth of crystallite size (50 nm) during carbonization process at 700 ˚C for 5 h.

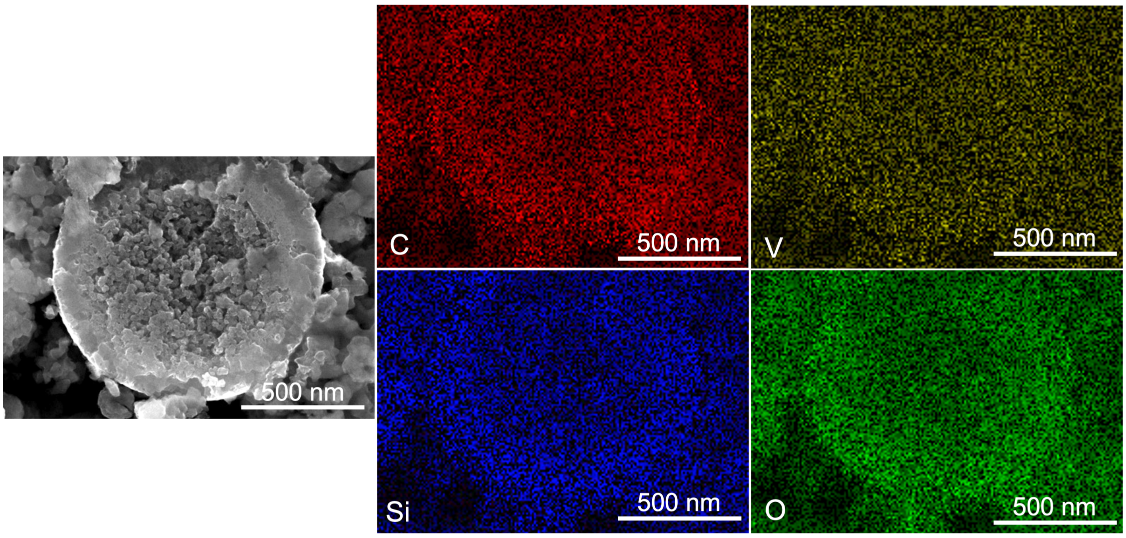

Fig. S2. SEM images and EDS elemental maps for the cross-section of the γ-LVSiO/C (as shown in Fig. 2b) prepared by spray drying with 30 wt% sucrose. Elemental maps of carbon, vanadium, silicon, and oxygen are shown in red, yellow, blue, and green, respectively.

SEM observation for the γ-LVSiO/C synthesized from liquid-phase γ-LVSiO precursors or high-solid content γ-LVSiO dispersion as a feed solution.

To elucidate the formation mechanism of the unique double capsule structure of γ-LVSiO/C (as shown in Fig. 2), two different types of feed solutions were spray-dried and SEM-observed (Fig. S3). In case of Fig. S3a, γ-LVSiO/C was synthesized from the liquid-phase feed solution of ionized γ-LVSiO precursors, containing the dissolved LiOH, V_2O_5, and SiO_2 powder reagents (mass of the resulting γ-LVSiO to be 1 wt%) in the sucrose aqueous solution (sucrose 30 wt%). The SEM image (Fig. S3a) clearly shows the hollow shell structure without any inside structure, which is similar to the OUTER SHELL structure as shown in the Fig. 2 and 3. On the other hand, the γ-LVSiO/C (Fig. S3b) synthesized from the feed solution containing solid-phase γ-LVSiO particles with high concentrations of 10 wt% in the sucrose aqueous solution (sucrose 30 wt%), exhibiting the huge aggregates without the outer shell structure. Such morphology is similar to the INNER PARTICLES of the γ-LVSiO/C synthesized from dilute dispersion of 1 wt% (as shown in Fig. 2), although the particle size is increased by excessive aggregation in high-solid content. These contrasting results clearly indicate that the IINNER PARTICLES and OUTER SHELL in the double capsule structure are obtained from solid grains of γ-LVSiO and liquid phase of the γ-LVSiO precursor, respectively.

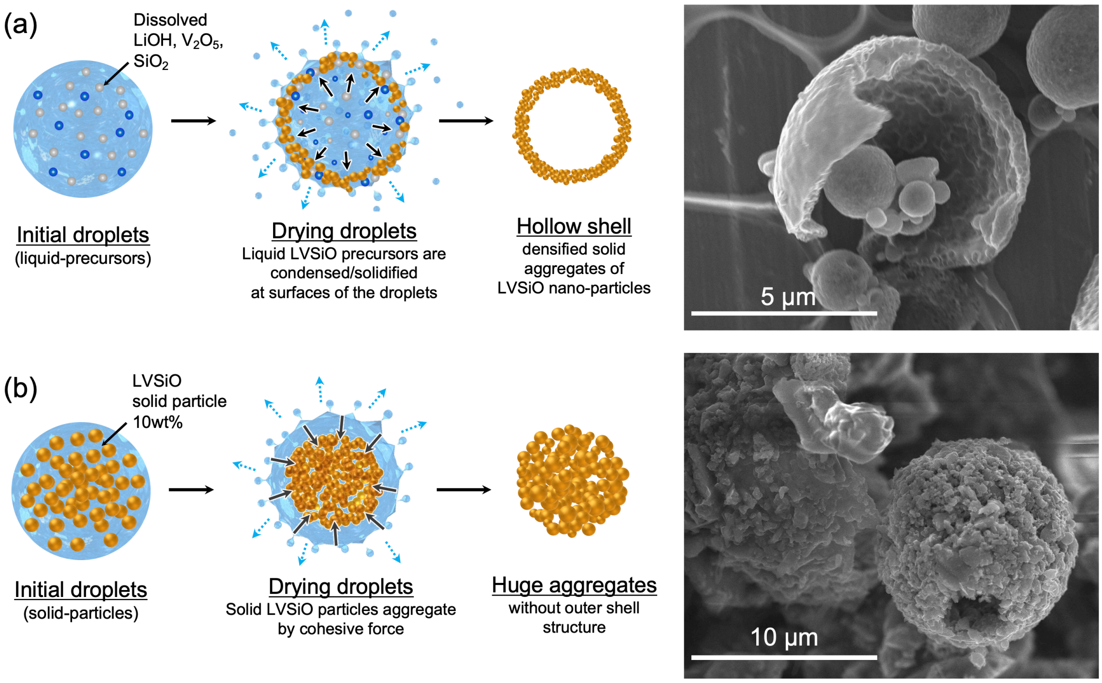

Fig. S3. SEM images for the γ-LVSiO/C synthesized in the two distinct spray-dry conditions of the feed solution with different nature: (a) Spray dry synthesis from the feed solution containing liquid-phase γ-LVSiO precursors prepared by dissolving LiOH, V_2O_5, and SiO_2 powder reagents (mass of the resulting γ-LVSiO to be 1 wt%) into the sucrose aqueous solution (sucrose 30 wt%). The sprayed droplets are subsequently ejected into a dry hot N_2 spiral turbulence at 160 °C, which instantly evaporates water from the droplet. The dissolved γ-LVSiO precursors are condensed/solidified at the droplet surfaces due to capillary action (indicated as black arrows), resulting in the hollow shell structure. SEM image for the collapsed γ-LVSiO/C shell clearly shows the hollow structure without any inner particles. (b) Spray dry synthesis from the feed solution containing solid-phase γ-LVSiO particles with high concentrations of 10 wt% in the sucrose aqueous solution (sucrose 30 wt%). In the sprayed droplets, solid γ-LVSiO particles aggregate by cohesive force (indicated as grey arrows), resulting in the huge aggregates without the outer shell structure, as confirmed in the SEM image.

NMR measurements for characterizing liquid-phase γ-LVSiO precursors

To confirm the nature of the γ-LVSiO dilute dispersion as an original feed solution for the spray dry synthesis, NMR measurements of ^{7}Li, ^{51}V, and ^{29}Si were conducted. The ionized Li, V, and Si spectra were obtained, indicating that the γ-LVSiO powder was partially dissolved and ionized in the sucrose aqueous solution. The observed ^{7}Li, ^{51}V, and ^{29}Si peaks were identified as a solvated Li^+, $H_xVO4^{(3-x)-}$, and $H_xSiO4^{(4-x)-}$ oligomers, respectively, corresponding to the peak shift value of references for ^{7}Li [6], ^{51}V [7], ^{29}Si [8].

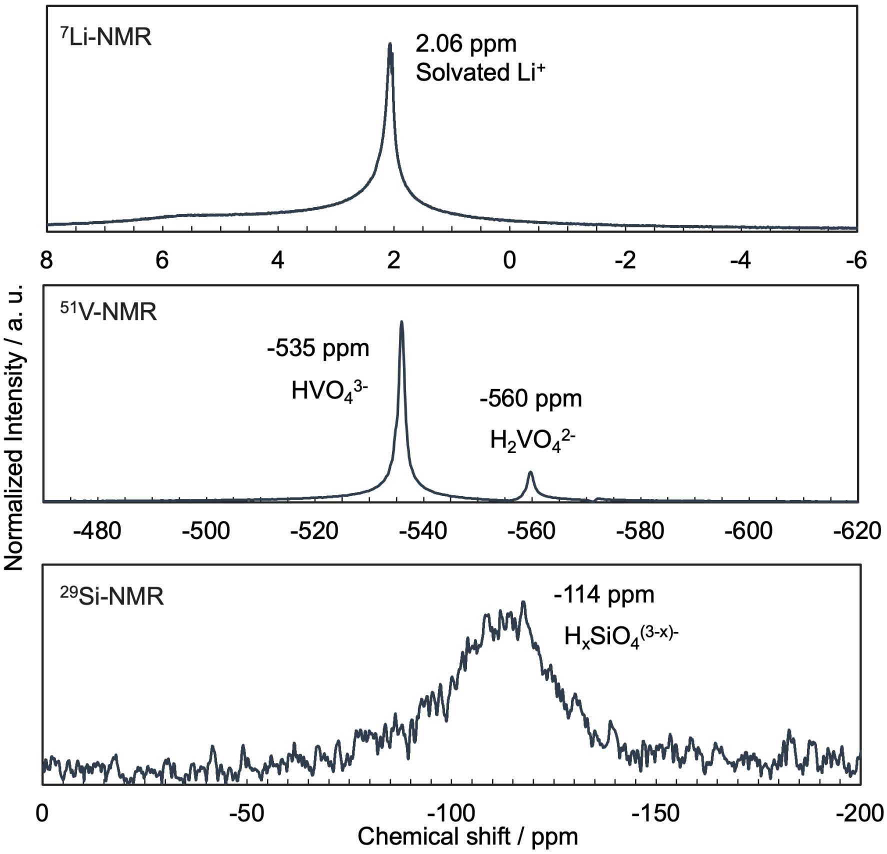

Fig. S4. NMR spectra of ^{7}Li, ^{51}V, and ^{29}Si for the γ-LVSiO dilute dispersion (solid content = 1wt%) as an original feed solution. The observed ^{7}Li, ^{51}V, and ^{29}Si peaks were identified as a solvated Li^+, $H_xVO4^{(3-x)-}$, and $H_xSiO4^{(4-x)-}$, respectively.

TG curves for other carbon materials:

To identify the carbons observed in TG weight loss for the γ-LVSiO/C in the two-temperature range of Region I (250–450 °C) and Region II (600–850 °C), TG measurements under synthetic air on three different carbons: graphite, Ketjen Black (KB) and sucrose-derived carbons in absence of the γ-LVSiO. Here, the three carbons were selected to see the dependency of combustion temperature range on the sp^2-characteristics of carbons. As shown in Fig. S5, TG weight losses for sucrose-derived carbon, KB, and graphite were observed around 450 °C, 650 °C, and 750 °C, respectively. These results demonstrate that the combustion temperature of carbon increases with an increment of the sp^2 characteristics of carbons (sucrose-derived carbon < KB < graphite). The combustion temperature range of the γ-LVSiO/C in 600–850 °C, denoted as "Region II" in Fig. 4a, lies between KB and graphite. Therefore, the second TG loss in Region II would correspond to the combustion of a partially ordered graphitic carbon phase. On the other hand, the lower combustion temperature in Region I indicates the existence of a more sp^3-like amorphous carbon phase.

Furthermore, TG curve for the sucrose-derived carbon shows the single combustion peak of amorphous carbon at 450 ˚C without any peaks of graphitic carbon (Fig. S5). The fact that the carbonized sucrose in the absence of γ-LVSiO combusted in Region I suggests that the γ-LVSiO crystals catalyse the graphitization.

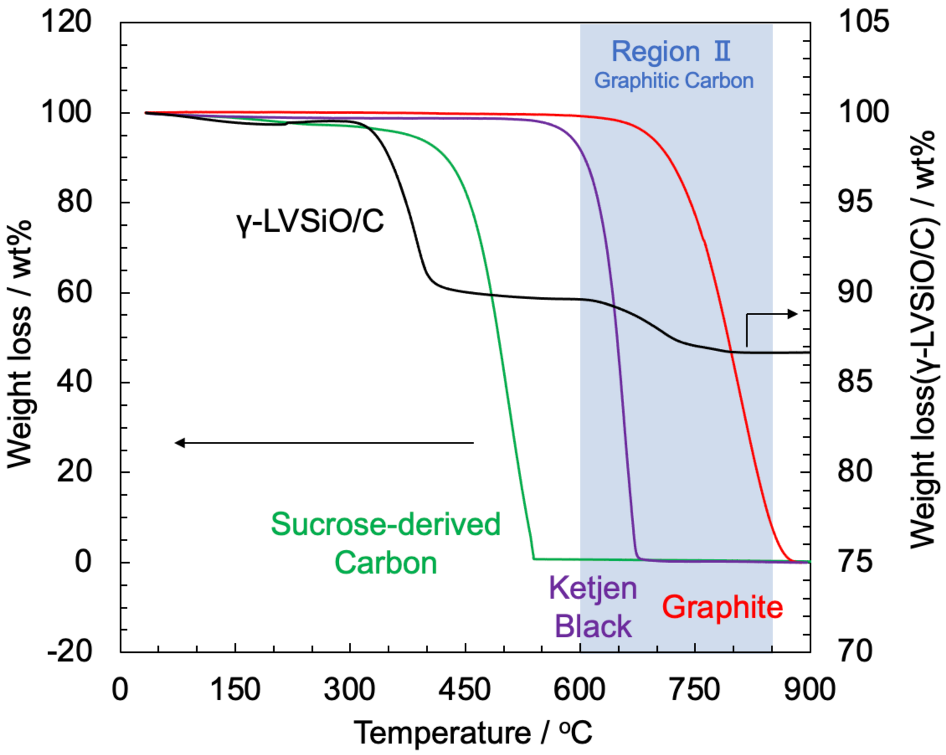

Fig. S5. TG curves for sucrose-derived carbon, Ketjen black, and graphite along with the γ-LVSiO curve, indicating combustion temperatures of each carbonaceous substances. The sucrose-derived carbon was synthesized by annealing sucrose granules in the same condition as the γ-LVSiO/C synthesis (700 °C; 5 h in N_2).

STEM images and EDS elemental mapping for the INNER PARTICLES in the γ-LVSiO/C capsule:

STEM image and with EDS elemental maps of carbon and vanadium with supplementary maps of silicon and oxygen (not shown in Fig. 4), focusing on the INNER PARTICLES of the γ-LVSiO/C are shown to confirm the elemental distribution (Fig. S6). The constituent elements of γ-LVSiO (vanadium, silicon and oxygen) are distributed in the same way, indicative of the existence of the γ-LVSiO crystals which are completely separated by connecting carbon phase.

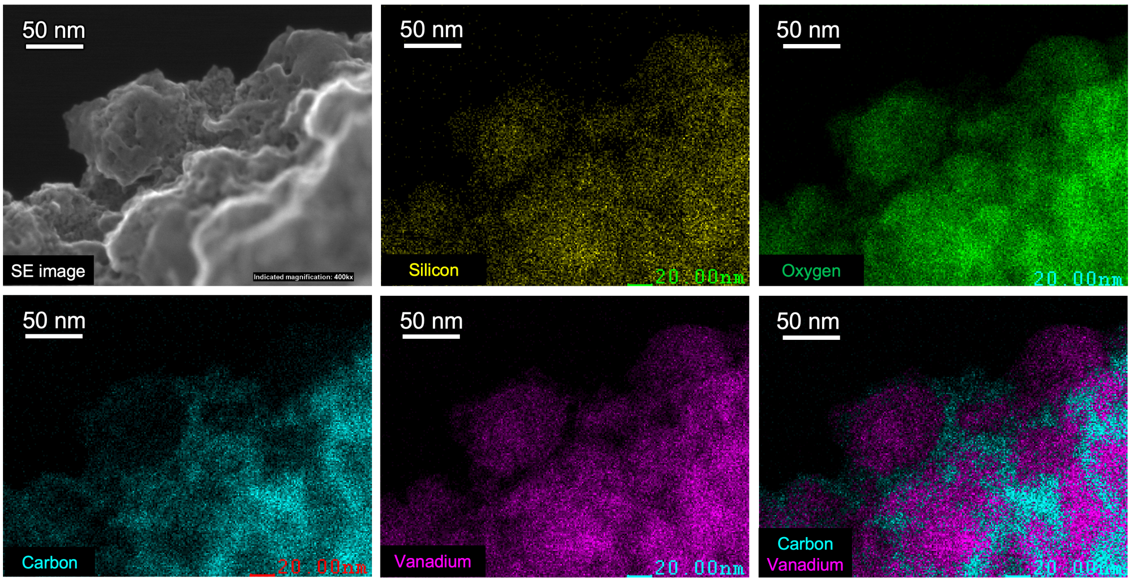

Fig. S6. HR-STEM image focusing on the INNER PARTICLES of the γ-LVSiO/C capsule (30 wt% sucrose) as shown in Fig. 4, with EDS elemental maps of carbon, oxygen, silicon, and vanadium. The constituent elements of γ-LVSiO (vanadium, silicon and oxygen) are distributed in the same way, indicative of the existence of the γ-LVSiO crystals which are completely separated by connecting carbon phase.

STEM images and EDS elemental mapping for the OUTER SHELL in the γ-LVSiO/C capsule:

The detailed structure of the OUTER SHELL (as shown in Fig. 2) was clearly revealed by STEM transmission images. Although, secondary electron (SE) image shows dense and smooth surface structure of the shell, annual dark field (ADF)- and bright field (BF)- STEM images revealed that the shell was constituted with the hollow or ring-shaped particles containing vacant space (Fig. S7). Enlarged SE-image and elemental maps focusing on the single particles of the shell clearly shows the hollow structure with uniform composition of V, Si, and O, indicating γ-LVSiO formation (Fig. S8). Only carbon was mapped in deferent region from the other elements. Combined image of ADF image and all elemental maps shows that the carbon exists independently to fill between particles (Fig. S8). Such hollow shell structure and carbon matrix may enable the fast diffusion of ions and electron conduction required for the high C-rate operation of active materials.

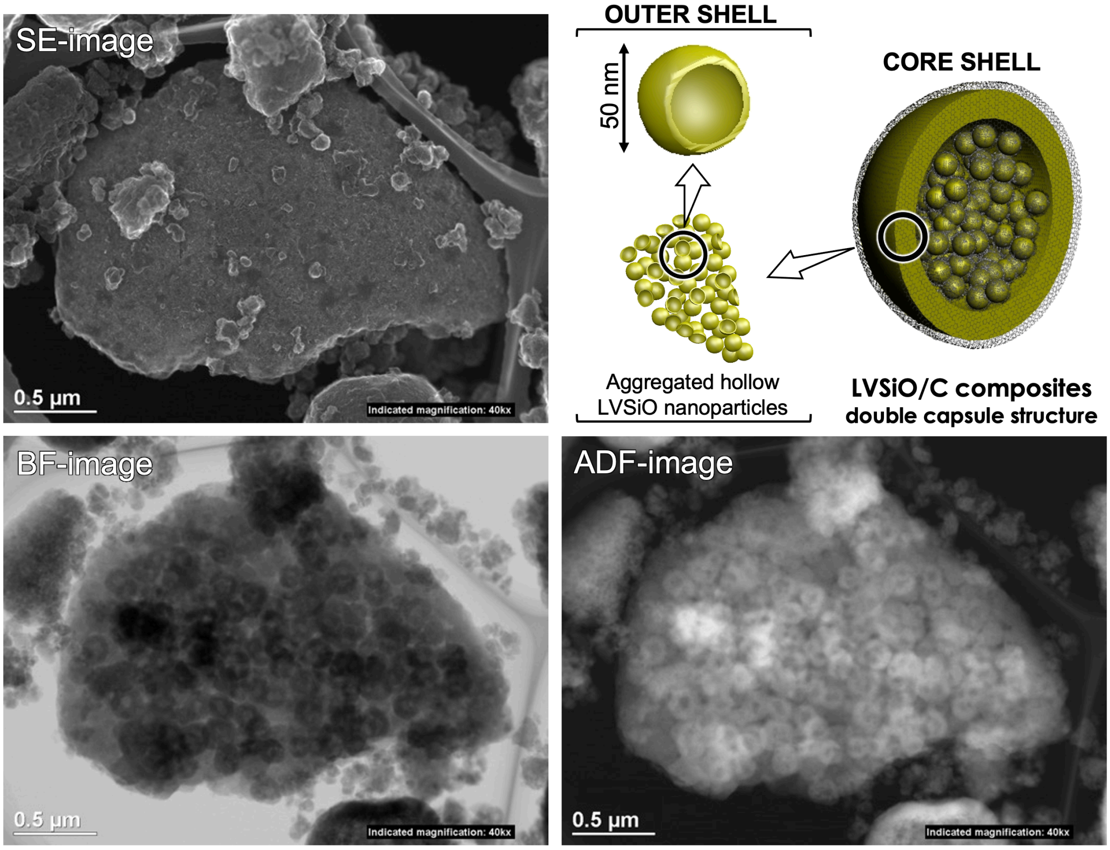

Fig. S7. HR-STEM images for the γ-LVSiO/C composites (Sucrose 30 wt%) focusing on the OUTER SHELL (as shown in Fig. 3). Secondary electron (SE) image displays the collapsed shell structure. Bright field (BF) and annular dark field (ADF) images clearly indicate that the OUTER SHELL is constituted with the aggregated hollow nanoparticles, as illustrated in the upper right. The interstices among the hollow nanoparticles are displayed as low contrast in the BF- and ADF-images, indicative of existence of relatively lighter elements than that of the hollow nanoparticles.

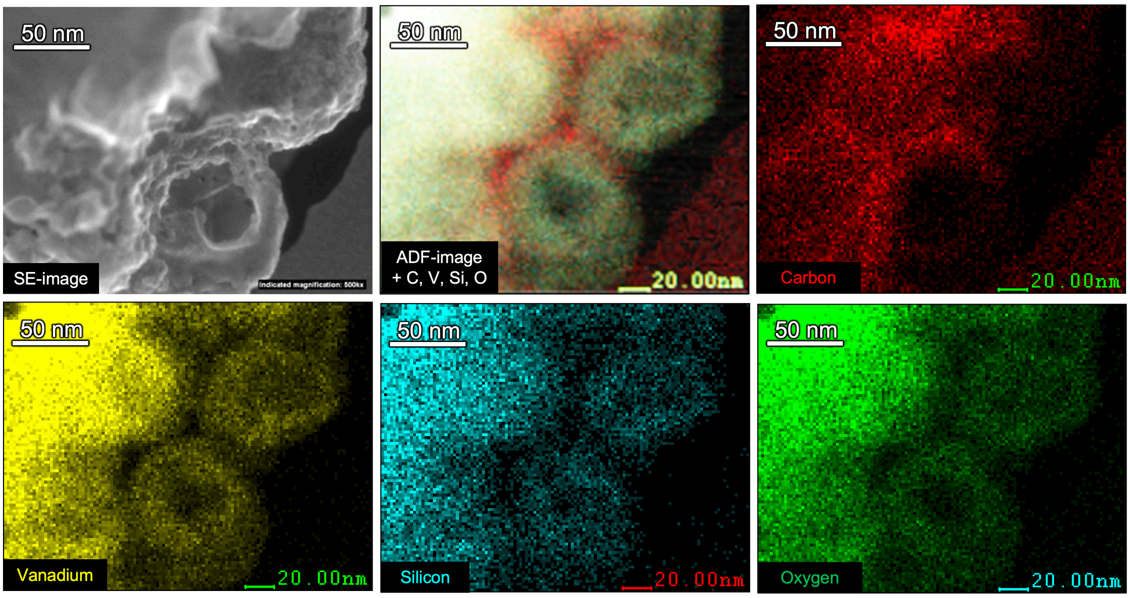

Fig. S8. HR-STEM images and EDS elemental maps for the γ-LVSiO/C composites (Sucrose 30 wt%) focusing on the constituent γ-LVSiO nanoparticle of the OUTER SHELL (as shown in Fig. S7). The SE-image together with the distribution of constituent element of γ-LVSiO (vanadium, silicon, and oxygen) displays hollow nanoparticles of γ-LVSiO (*ca.* 50 nm). The combined image of the ADF-image with all elemental maps clearly suggests the existence of the carbon independently to fill the particles interstices.

XRD pattern of P-substituted $Li_{3.2}P_{0..8}Si_{0.2}O_4$:

To confirm crystal structure of P-substituted γ-$Li_{3.2}P_{0.8}Si_{0.2}O_4$ (γ-LPSiO) synthesized by the solid-state reaction, XRD measurement was performed. XRD patterns of the γ-LPSiO and the γ-LVSiO were indexed as the same γ-phase crystal structure (space group: *Pnma*), indicating successful synthesis of γ-LPSiO (Fig. S9).

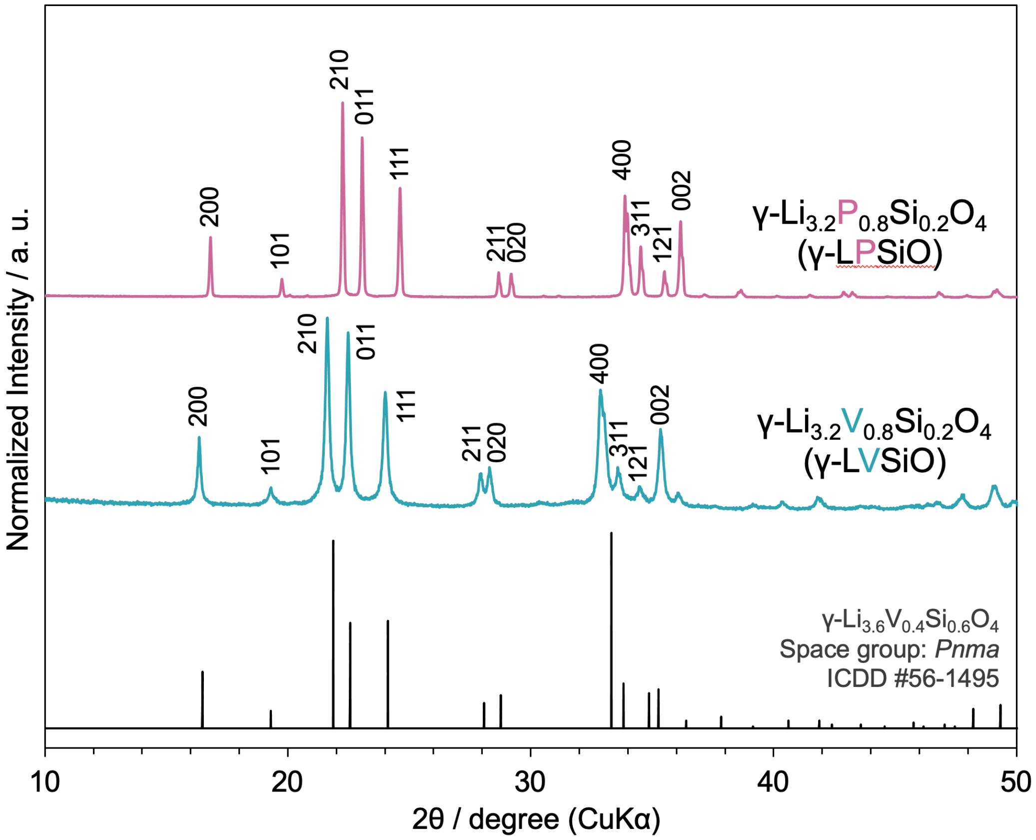

Fig. S9. XRD patterns of P-substituted γ-LPSiO/C and γ-LVSiO/C synthesized by the spray dry method were indexed as the same γ-phase crystal structure whose space group was *Pnma*.

XPS measurements for γ-LVSiO/C and γ-LPSiO/C:

To evaluate the interaction between the vanadium and the carbon phases, XPS measurements were made for the γ-LVSiO/C and γ-LPSiO/C. As shown in Fig. S10, it is clearly found that C–V bond (282 eV) is existed neither for γ-LVSiO/C nor γ-LPSiO/C, indicating that the crystal phase and the grown carbon phase are completely separated without having any direct C–V covalent bonds. Rather, the clear peak attributed to C–O or C=O bonds around 289 eV can be found for the γ-LVSiO/C, while its intensity is negligible for the γ-LPSiO/C. The results indicate the existence of the chemical interaction between the carbon and oxygen atoms of the γ-LVSiO crystal surface to form C–O–V bonds, as shown in Fig. S11. The formation of C–O–V bonds may initiate a nucleation of carbon species, resulting in an arrangement of a carbon layer along the surface profile of γ-LVSiO crystals. Such arranged carbon layer on the γ-LVSiO crystals surface induces a few (2–4 layers) of carbon layer stacking to form the graphitic carbon. The reason why only γ-LVSiO forms such C–O–V bonds may be the difference in covalency (ionicity) between V-O (γ-LVSiO) and P-O (γ-LPSiO) dangling bonds; The O atoms in less covalent V–O may interact with C atoms in a sucrose molecule to form C–O–V bond compared to the strong covalent P–O bond.

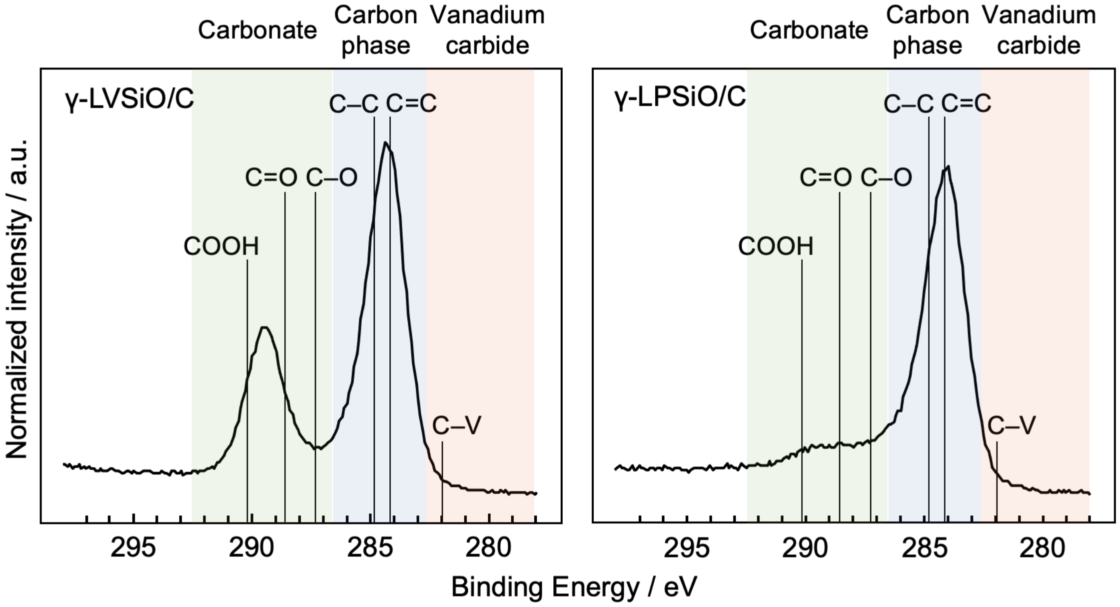

Fig. S10. C*1s* XPS spectra for γ-LVSiO/C and γ-LPSiO/C with reference peak positions of vanadium carbide, carbon phase, and carbonate species [9-11]. The γ-LVSiO/C spectra clearly show the two peaks at 284 eV and 289 eV, corresponding to the C–C or C=C bonds and oxidated carbon peaks (C–O, C=O, or COOH bonds), respectively, without any C–V bonding. In contrast, the γ-LPSiO/C spectra mainly shows C–C or C=C bonds with negligible carbonate peaks.

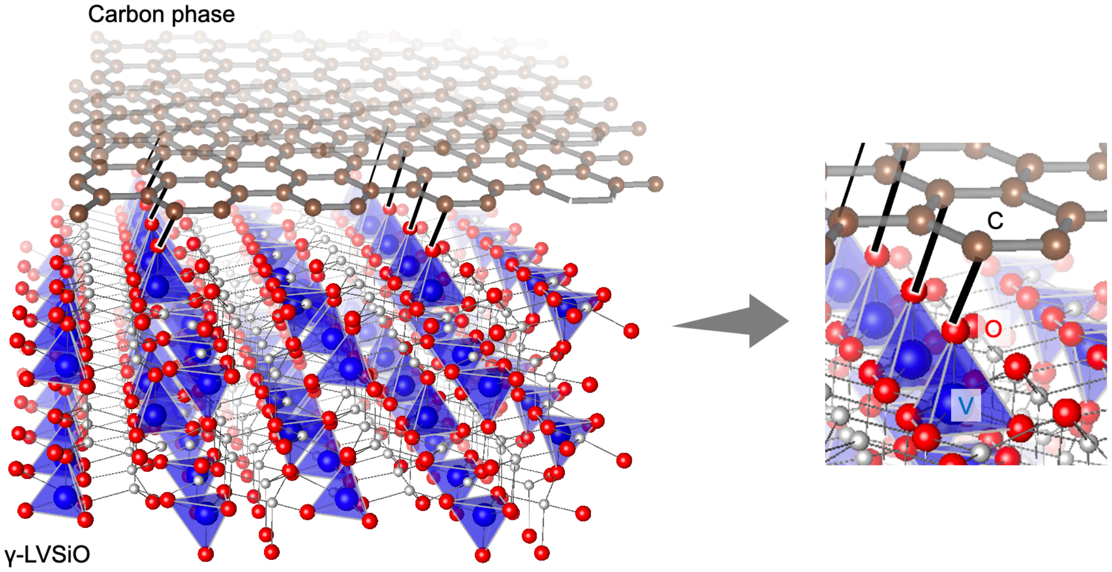

Fig. S11. Schematic images of arrangement of a carbon layer along with the surface of γ-LVSiO crystal owing to the possible C–O–V bonds.

ESR spectroscopy for detecting tetravalent V ions:

Electron spin resonance spectroscopy (ESR) can detect trace amount of V^{4+} that has an unpaired *d*-electron. As shown in Fig. S12a, the ESR spectrum characteristic of V^{4+}, whose parallel and perpendicular component each split due to the ^{51}V nuclear spin (I=7/2), was observed for the spray-dried power of the γ-LVSiO/C precursors before carbonization[12]. In contrast after carbonization, the V^{4+} was clearly diminished and the single resonance line, which is typical to conductive graphitic carbon[13] (Fig. S12b). The *d*-electron of V^{4+} may back-donate to the antibonding π^* orbitals of C=C, thereby improving the affinity between V^{4+} and the sp^2 carbon. This stabilization effect between the sp^2 carbon and the γ-LVSiO surface lowered the activation energy and temperature of graphitization.

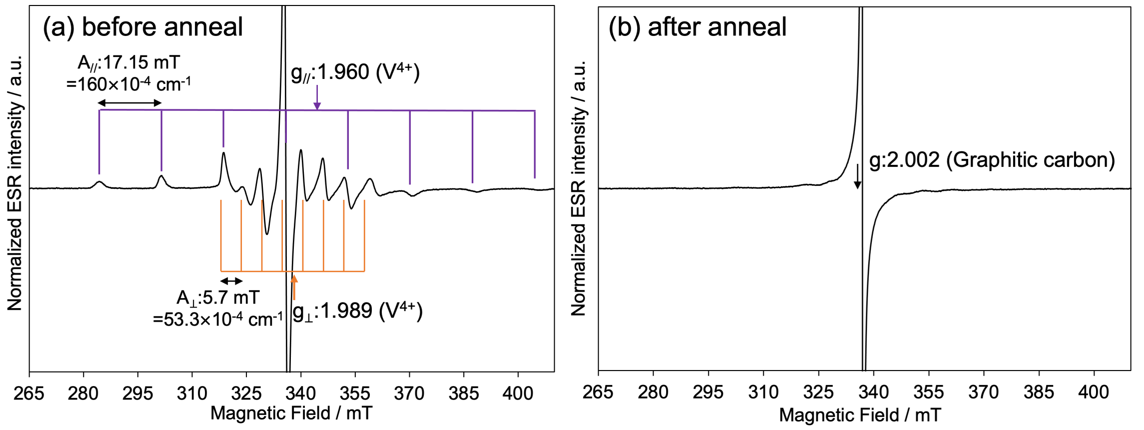

Fig. S12. ESR spectra of the spray-dried γ-LVSiO with sucrose 30 wt% (a) before and (b) after annealing, where g and A are the anisotropic g-factor and the hyperfine coupling parameter, respectively. (a) The split ESR peaks typical of V^{4+} with parallel (g = 1.960) and perpendicular component (g = 1.989) was detected before annealing. (b) The peaks of V^{4+} clearly disappeared and another ESR peak specific to the graphitic carbon (g = 2.002) appeared.

Comparison of crystallinity and crystallite size of γ-LVSiO at different sucrose contents:

γ-LVSiO/C composites with various amounts of carbon were synthesized using different dosages of sucrose as the carbon source. To evaluate the crystallinity of these samples, XRD measurements were performed. As shown in Fig. S13, all XRD patterns were indexed to the space group *Pnma* of the of the γ-phase $Li_{3.6}V_{0.4}Si_{0.6}O_4$ (ICDD #56-1495), indicating the successful synthesis of γ-LVSiO crystals with various sucrose dosage.

The crystallite size and its average were calculated from the FWMH of XRD peaks, corresponding to 200, 020, and 002 reflections, by using the Scherrer equation[4] (eq. S1) (Table S2). The crystallite size was also estimated by the Halder-Wagner method[14]. The calculated crystallite sizes decreased with an increase of sucrose dosage up to 30 wt%. Among three samples of Suc. 30-50 wt%, After a slight increase from Suc. 0 to Suc. 10 wt%, the average crystallite size continuously decreased with an increase of sucrose dosage up to 30 wt% (Suc. 30 wt%), while that became constant over 30 wt%. These results suggest that the particle growth during annealing at 700 ˚C was inhibited by carbonized sucrose, and the 30 wt% dosage was enough to cover almost all the surfaces of the 1 wt % of ball-milled γ-LVSiO particles.

Table S2. Comparison of the full width of half maximum (FWHM) of XRD peaks and crystallite size of γ-LVSiO/C composites prepared with various sucrose amount.

	FWHM/ deg			Crystalline size / Å				
	200	020	002	200	020	002	Average	Halder-Wagner
Suc. 0 wt%	0.1042(15)	0.117(2)	0.1293(14)	804(11)	733(15)	674(7)	737(7)	795(65)
Suc. 10 wt%	0.090(3)	0.115(4)	0.119(9)	934(28)	744(23)	731(53)	803(21)	813(69)
Suc. 20 wt%	0.072(3)	0.0206(6)	0.186(18)	1164(43)	416(12)	469(45)	683(21)	451(56)
Suc. 30 wt%	0.094(4)	0.241(12)	0.201(14)	892(41)	355(18)	434(31)	560(18)	313(63)
Suc. 40 wt%	0.110(5)	0.271(12)	0.198(13)	762(37)	316(14)	441(29)	506(16)	346(56)
Suc. 50 wt%	0.085(5)	0.318(16)	0.23(3)	987(55)	269(14)	385(46)	547(24)	269(51)

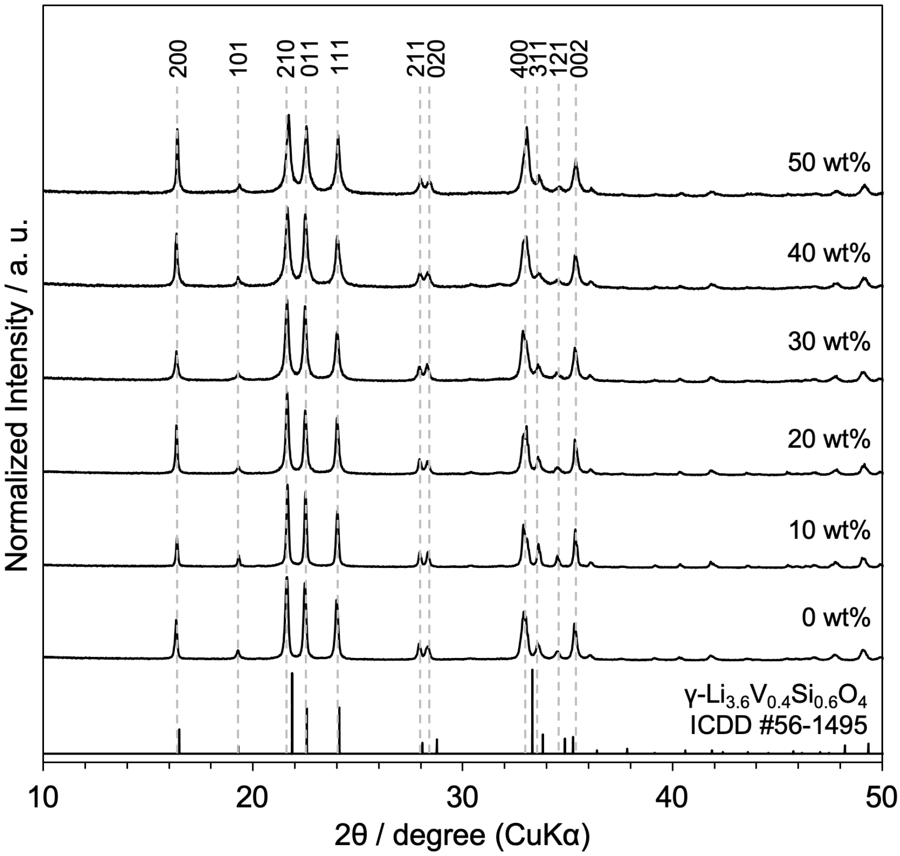

Fig. S13. XRD patterns for the γ-LVSiO/C composites synthesized from six types of feed solutions with different sucrose dosage in concentration of 0–50 wt%. All XRD patterns are indexed as the space group *Pnma* of the of the γ-phase structure, with reference to γ-$Li_{3.6}V_{0.4}Si_{0.6}O_4$ (ICDD #56-1495). The FWHM of the XRD patterns increases with increase in the sucrose dosage, which are summarized in Table S2 with calculated crystallite size.

Charge/discharge profiles for the γ-LVSiO/C (sucrose 30 wt%) during initial 20 cycles

Fig. S14 shows representative charge-discharge profiles of γ-LVSiO/C (Suc. 30 wt%) at 0.1 A g^{-1} during initial 20 cycles. The dominant pseudocapacitive slope observed in 0.4–1.3 V *vs.* Li corresponds to the reaction potential of γ-LVSiO[15, 16], while an irreversible plateau around 0.7 V vs. Li corresponding to the electrolyte decomposition appeared only at the first cycle. In contrast to β-phase LVO, irreversible profile change is not seen in the profiles of γ-phase γ-LVSiO, indicating its high reversibility without any crystal change such as cation-disordering,[5, 17]. The obtained capacity at the 20th cycle was ~288 mAh g^{-1}, which is 103% of its theoretical capacity (279 mAh g^{-1}) considering the 20% Si^{4+} substitution of active V^{5+} and the presence of 12.4 wt% of carbon. This result suggests that almost all the γ-LVSiO crystals are electrochemically active, meaning that electronic and ionic paths are sufficiently formed in the composites.

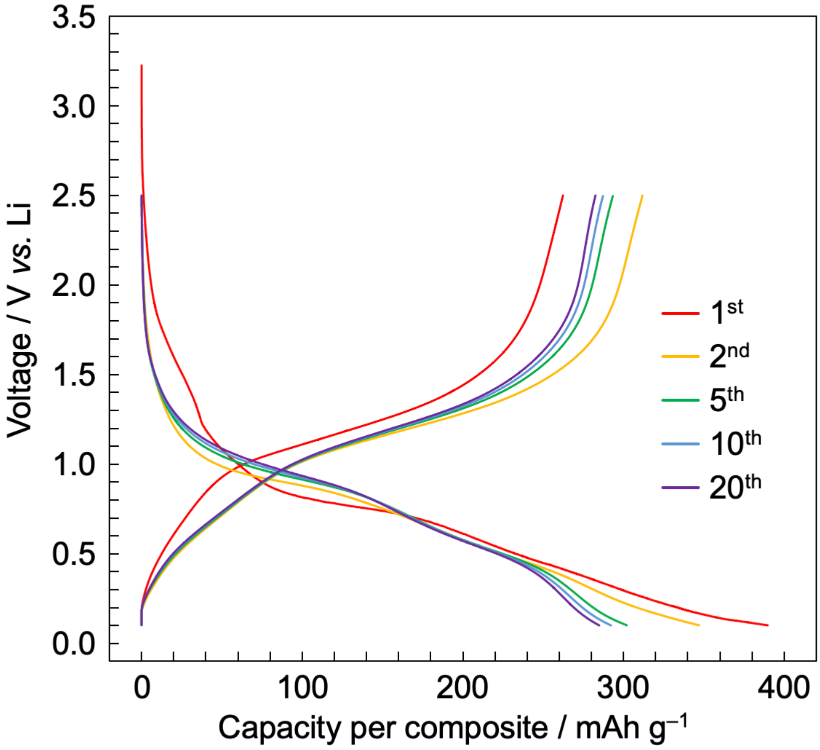

Fig. S14. Charge/discharge profiles for 20 cycles of a half-cell consisting of Li/1 M $LiPF_6$ EC + DEC (vol 1:1)/γ-LVSiO/C (synthesized in 30 wt% of sucrose dosage) at 0.1 A g^{-1}.

Full spectrum of electrochemical characteristics in the rate-performance tests:

The rate performance data relative to the charging behaviors were supplemented to understand the full spectrum of electrochemical characteristics, featuring high-rate performance. The charge (delithiation) curves of Suc. 10wt%, Suc. 30 wt% and Suc. 50 wt% samples at different charge current densities are shown in Fig. S15 as representative of the typical cases of insufficient (2.5 wt%), optimal (9.5 wt%) and excess (19.2 wt%) amorphous carbons, respectively. First, the curve of Suc. 10 wt% did not exhibit any capacity due to the large polarization, even at a low current density of 0.1 A g^{-1}, indicating lack of electronic connections between γ-LVSiO particles. In contrast, the charge curve of Suc. 30 wt% and Suc. 50wt% at 0.1 A g^{-1} shows sloping charge discharge behaviors with exhibited capacity of 288 and 230 mAh g^{-1}, respectively. The obtained capacity of Suc. 30 wt% samples corresponds to 103% of its theoretical capacity, according to the two-electron reaction of V^{5+}/V^{4} and V^{4+}/V^{3+}. In light of the reaction states, two reaction regions can be seen in the charge curve of the γ-LVSiO: (i) a steep sloping region at 0.5–1.0 V *vs.* Li corresponding to the redox of V^{4+}/V^{3+} and (ii) a gentle sloping region at 1.0–1.5 V *vs.* Li corresponding to the redox of V^{5+}/V^{4+}. Comparing the charge curves of Suc. 30 wt% and Suc. 50 wt% samples at increased charge current densities, IR drop and diffusion overpotential were drastically increased in the Suc. 50 wt%. Such large IR drop and diffusion overpotential leads to the capacity decrease at high C-rates, due to the loss of gentle sloping reaction region of V^{5+}/V^{4+} at the cut-off potential of 2.5 V *vs.* Li. Thus, the Suc. 50 wt% samples exhibited small capacity of 34 mAh g^{-1} for at 10 A g^{-1}. On the other hand, the charge curve of the Suc. 30 wt% maintains its gentle sloping region even at high rate of 5 A g^{-1} with the relatively low IR drop. The curve steepens at 10 A g^{-1}, but still keeps the gentle sloping profile as the results at the lower rates, resulting in a larger capacity of 199 mAh g^{-1} for the Suc. 30 wt% at 10 A g^{-1}. Such drastic improvements of the rate performance is owing to the optimizing the pore-structure for electrolyte diffusion determined by the amorphous carbon content, as discussed in the EIS measurements (Fig. 9) and the N$_2$-adsorption measurements (Fig. S16).

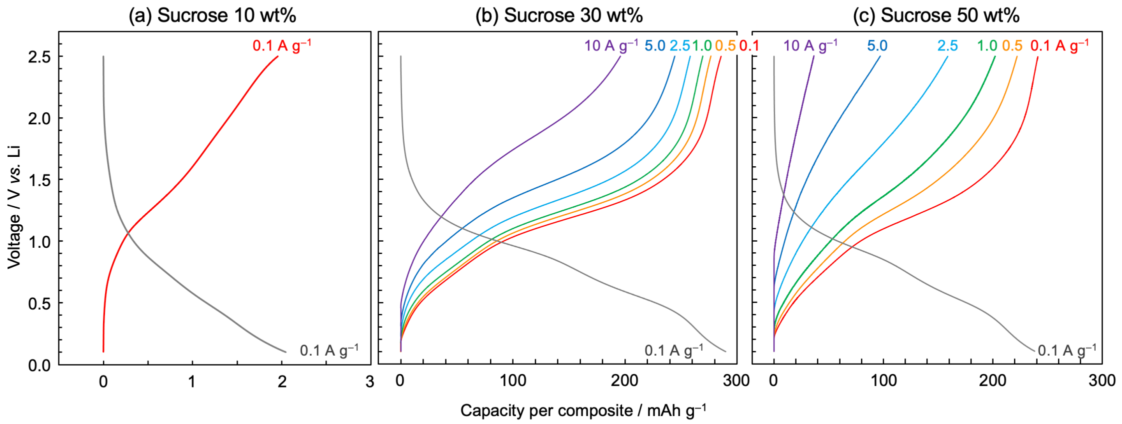

Fig. S15. Charge (delithiation) profiles of (a) Suc. 0 wt%, (b) Suc. 30 wt% and (c) Suc. 50 wt% at different charge current densities of 0.1, 0.5, 1.0, 2.5, 5.0, and 10 A g^{-1} and constant discharge current densities of 0.1 A g^{-1} shown in gray. The Suc. 0wt% sample shows almost no charge/discharge capacity (2 mAh g^{-1}) even at low-current density of 0.1 A g^{-1}.

Specific BET surface area and pore distribution for the γ-LVSiO/C:

Change in pore distribution for the γ-LVSiO/C relative to the carbon amount was investigated by nitrogen adsorption-desorption with the Barrett-Joyner-Halenda (BJH) plots (Fig. S16). With increasing sucrose dosage, the volume adsorbed in the high-pressure region and the pore volume (ϕ > 10 nm) was decreased, indicating that the increased carbon filling the porous structure. Based on the Brunauer-Emmett-Teller (BET) theory, the specific surface area of the γ-LVSiO/C (sucrose dosage 10, 30, 50 wt%) were estimated as 6.8, 4.4, 24.0 m^2 g^{-1}, respectively. These results suggest that the interstices in the γ-LVSiO/C composites are filled with the amorphous carbon with increase in the sucrose dosage up to 30 wt%, leading to decrease in the surface area. Meanwhile, most of the pore structure are filled with the excess amount of amorphous carbon (over 30 wt% of sucrose), which have mesopores (ϕ < 10 nm), resulting in the small pore volume and larger surface area. Such mesoporous structure were confirmed by the isotherm of sucrose 50 wt% sample with hysteresis and large adsorption volume in the region of 0.2–0.8 relative pressure.

As illustrated in Fig. S16b, an optimal amount of amorphous carbon (sucrose 30 wt%) constructs continuous carbon network with porous structure, resulting in both electronic conduction pathways and electrolyte reservoirs/diffusion pathways. On the other hand, shortage of amorphous carbon (sucrose 10 wt%) causes disconnection of the carbon network for the electronic conduction. Excessive carbon (sucrose 50 wt%) fills the pores in the composite structure.

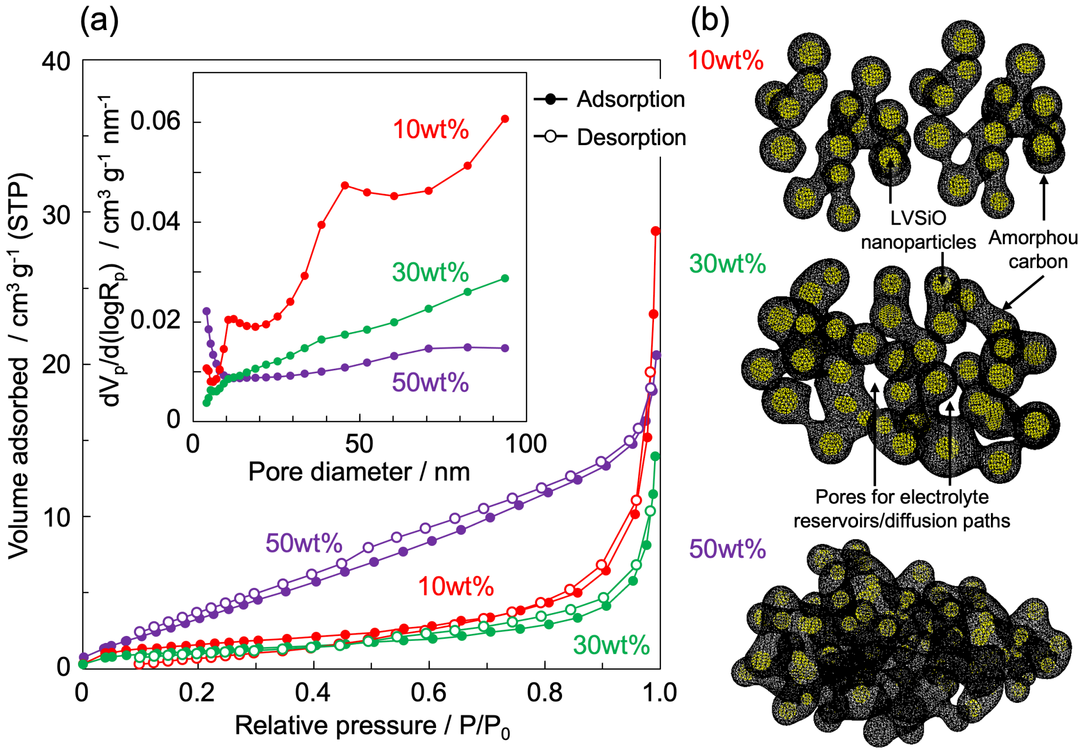

Fig. S16. (a) Nitrogen adsorption (closed circle) and desorption (open circle) isotherms of the γ-LVSiO/C (synthesized in 10, 30, and 50 wt% of sucrose dosage). Based on the Brunauer-Emmett-Teller theory, the specific surface area of the sucrose 10, 30, 50 wt% samples were estimated to be 6.8, 4.4, 24.0 m^2 g^{-1}, respectively. The Barrett-Joyner-Halenda plots shown in the inset clearly demonstrate that the pores volumes ($\phi > 10$ nm) decreased with increase in the sucrose dosage. (b) Schematic illustration for the change in morphology of the γ-LVSiO/C with increase in the carbon content. An optimal amount of amorphous carbon (sucrose 30 wt%) constructs continuous carbon network with pores existing in the interstices for electrolyte reservoirs/diffusion paths. A shortage of amorphous carbon (sucrose 10 wt%) causes disconnection of the carbon network for the electronic conduction. Excessive carbon (sucrose 50 wt%) fills the pores in the composite structure.

The contribution of graphitic carbon on electronic conduction:

The electrochemical contribution of the graphitic carbon on the γ-LVSiO/C was evaluated by comparing the γ-LVSiO/C with/without the graphitic carbon (sucrose dosage 10 wt% and 0 wt%). Since there was no amorphous carbon, 0.2 wt% of single-walled carbon nanotubes (SWCNTs) with a high aspect ratio were added to ensure a long electron conduction. As shown in Fig. S17 (left), sucrose 10 wt% samples exhibited the larger capacity and superior rate performance than sucrose 0 wt% samples, indicative of the more γ-LVSiO crystals to be electrochemically active due to the graphitic carbon. These results suggest that the graphitic carbon imparts the electron conduction to the surface of γ-LVSiO particles, improving the utilization of active materials with minimal conductive agents, as depicted in Fig. S17 (right).

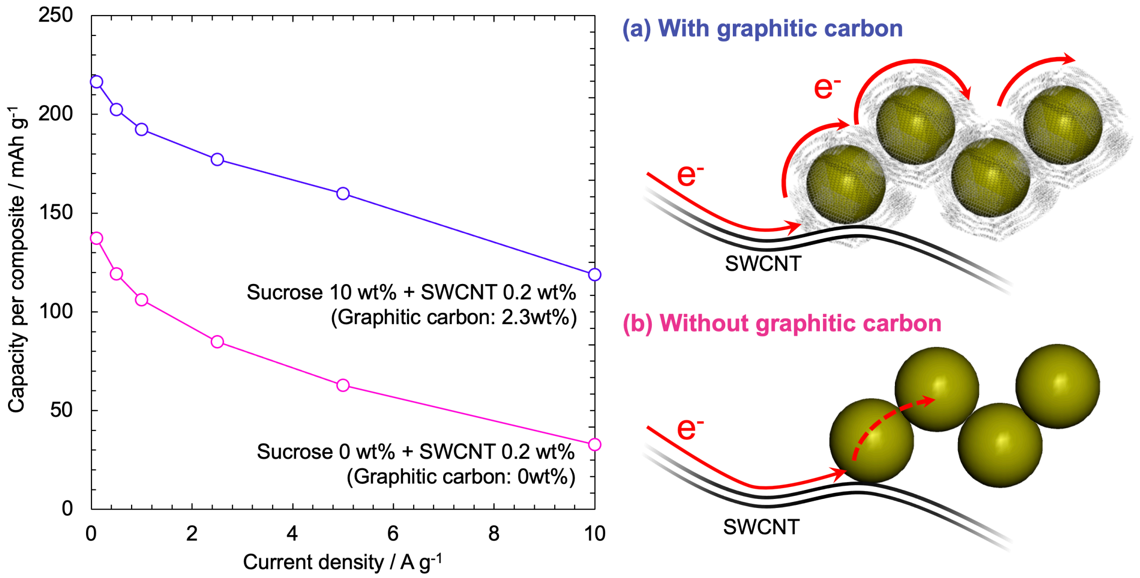

Fig. S17. The electrochemical contribution of the graphitic carbon of the γ-LVSiO/C. (Left) Rate performances (delithiation) of γ-LVSiO/C synthesized with 0 or 10 wt% of sucrose dosage, which mostly carbonize into the graphitized phase. Single-walled carbon nanotubes (SWCNT) are added as a long-range electronic conduction, instead of the amorphous carbon. (Right) Schematic illustrations of the effect of graphitic carbon where active material particles (yellow balls), graphitic carbon (black layer), electronic pathways (yellow line) and SWCNT (black line) are shown. (a) Sucrose 10 wt% samples with SWCNTs that include the graphitic carbon layers, where electrons conduct on the surface of the particles. (b) Sucrose 0 wt% samples with SWCNTs that has the no graphitic carbon where only particles contacted with SWCNT are electrochemically active.

Charge and discharge profiles for the $Li_3V_2(PO_4)_3$/MWCNT cathode:

$Li_3V_2(PO_4)_3$ (LVP) material was synthesized *via* a unique ultracentrifugation (uc) technique [18]. The uc-treated LVP contains highly crystalline LVP nanoparticles (diameter = 10–100 nm), which are highly dispersed within a MWCNT matrix. As shown in Fig. S18, the LVP cathode exhibits typical three-step plateaus. Observed three voltage plateaus in the charge discharge profiles for the full cells (Fig. 10) are originated to the plateaus of the LVP.

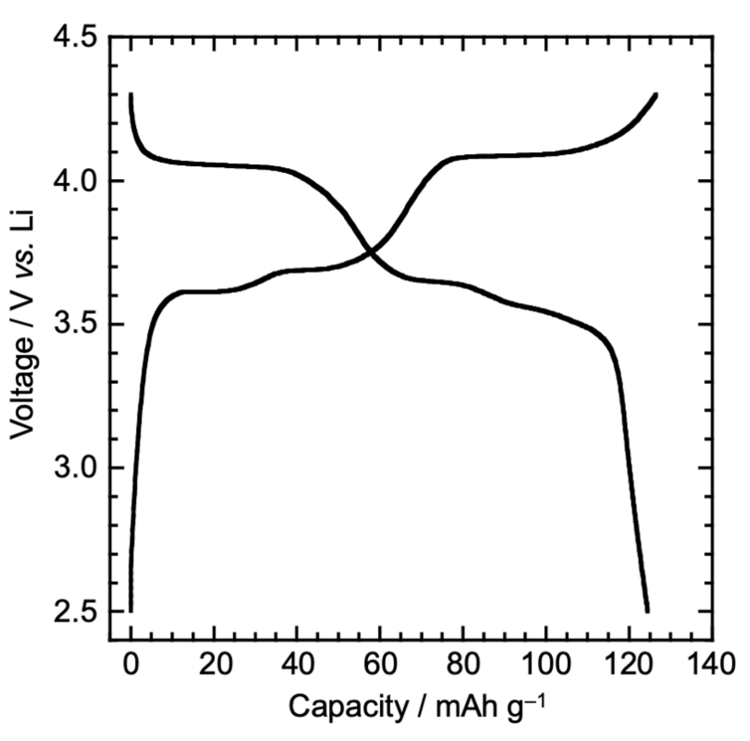

Fig. S18. Charge/discharge profiles of a half-cell composed of Li-metal / 1.0 M $LiPF_6$ in EC/DEC (1/1 in volume) / uc-$Li_3V_2(PO_4)_3$/MWCNT operating in a range of 2.5–4.3 V *vs.* Li at 1C-rate (131.5 mA g^{-1}).

Ragone plot for the γ-LVSiO/C//$Li_3V_2(PO_4)_3$/MWCNT full cell:

As shown in Fig. S19, we prepared the Ragone plots for the 0.4-mAh-class full cell of γ-LVSiO//$Li_3V_2(PO_4)_3$ (LVP) with other reported LVO-based-battery full cells as well as supercapacitors composed of two activated carbon (AC) electrodes, and hybrid supercapacitors of $Li_4Ti_5O_{12}$(LTO)//AC and LVO//AC.

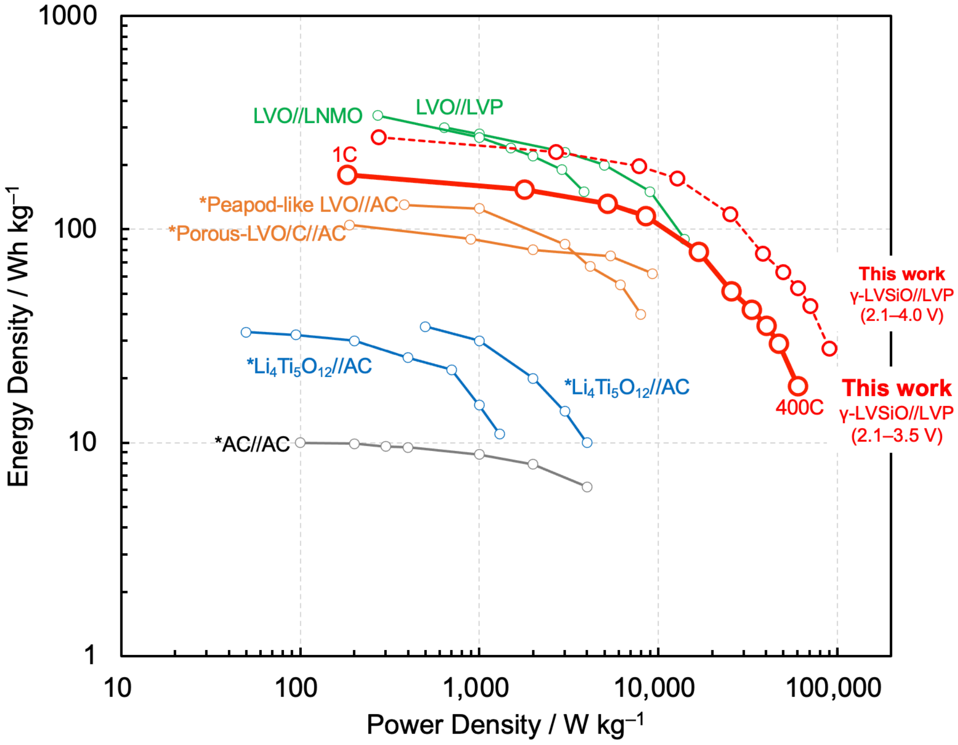

Fig. S19. Ragone plots for the 0.4 mAh-class laminate-type cells composed of γ-LVSiO/C//uc-$Li_3V_2(PO_4)_3$/MWCNT (γ-LVSiO//LVP), and other reported energy storages. **[Red line]** Result of the rate-performance test for γ-LVSiO//LVP full cell operated in a limited voltage range of 2.1–3.5 V (Fig. 10d). **[Red-dotted line]** Simulated Ragone plot for our full cell with utilizing full-reaction range for the γ-LVSiO anode (1.2–0.1 V *vs.* Li), operated in a full voltage range of 2.1–4.0 V. **[Grey and blue lines]** Plots for conventional supercapacitor (AC//AC)[19] and hybrid supercapacitor ($Li_4Ti_5O_{12}$//AC)[19, 20]. **[Orange lines]** Plots for reported LVO-based hybrid supercapacitors of porous-LVO/C//AC[21] and peapod-like LVO//AC[22]. **[Green lines]** Plots for LVO-based Li-ion batteries of LVO//$LiNi_{0.5}Mn_{1.5}O_4$ (LNMO)[23] and LVO// LVP[24], which were operated in voltage range of 2.2–4.5 V and 1.0–4.5 V, respectively. The * symbols stand for the data based on total weight of both electrodes.

First, we prepared two types of plots for the LVSiO//LVP full cells with different voltage range; i) plots with red solid line correspond to the experimental data for LVSiO//LVP full cell operated within a voltage range between 2.1 and 3.5 V, and ii) simulated plots with an enlarged voltage range between 2.1 and 4.0 V.

The LVSiO//LVP full cells i) 2.1-3.5 V were specially designed for commercial use in micro power recovery systems in photovoltaic systems. Limited operating voltage range 2.1-3.5 V was selected to achieve enough stability, feasibility, and high energy efficiency for such application. By limiting voltage range of full cells, *i.e.*, sacrificing its capacity, the operation potential range of γ-LVSiO is limited within 0.6–1.2 V *vs.* Li. In such operation potential range, the full-cell capacity degradation over 1,000 cycles can be minimized as shown in Fig. 10 owing to the minimized shift of state of charge (SOC) between LVSiO and LVP electrodes. Thus, in order to fulfill fair comparison with other LVO-based full cells, we simulated another Ragone plot of γ-LVSiO//LVP full cell ii), assumed to be operated in the full voltage operation range (2.1-4.0 V).

As shown in Fig. S19, the γ-LVSiO//LVP full cell with different operating voltage ranges exhibited a high energy density of 180–270 or 120–180 W h $kg^{-–1}$ at 1C-rate based on the mass of the anode material or the sum of anode and cathode materials, respectively, which surpassed the energy density of AC//AC, LTO//AC, and LVO//AC. Those energy values of γ-LVSiO//LVP i) are relatively smaller than those of LVO-based-batteries such as LVO//LNMO and LVO//LVP systems, which utilize the all the capacity of LVO without limiting operation potential range. Meanwhile, our γ-LVSiO//LVP i) exhibited ultrafast performance equivalent to 400C-rate (discharge in 9 s), and high energy density of 100 Wh kg^{-1} was maintained at ultrahigh power density of 10 kW kg^{-1}, which significantly outperformed other studies. Then, the simulated plots ii) with full operation voltage range shows comparable energy density with LVO-based-batteries, and still outperforms them in terms of power density. Accordingly, the two Ragone plots of γ-LVSiO//LVP full cell i) and ii) show their promising electrochemical performances compared to other reports/devices.

References

1. J. Xu, P. Liang, D. M. Zhang, C. Y. Pei, Z. P. Zhang, S. Y. Yang and S. B. Ni, *Journal of Materials Chemistry A*, 2021, **9**, 17270-17280.
2. Q. D. Li, J. Z. Sheng, Q. L. Wei, Q. Y. An, X. J. Wei, P. F. Zhang and L. Q. Mai, *Nanoscale*, 2014, **6**, 11072-11077.
3. P. Scherrer, *Mathematisch-Physikalische Klasse*, 1918, **2**, 98-100.
4. J. I. Langford and A. J. C. Wilson, *J. Appl. Crystallogr.*, 1978, **11**, 102-113.
5. P. Rozier, E. Iwama, N. Nishio, K. Baba, K. Matsumura, K. Kisu, J. Miyamoto, W. Naoi, Y. Orikasa, P. Simon and K. Naoi, *Chem. Mater.*, 2018, **30**, 4926-4934.
6. J. W. Akitt and A. J. Downs, *Chem. Commun.*, 1966, DOI: 10.1039/C19660000222, 222-224.
7. D. Rehder, T. Polenova and M. Bühl, in *Annual Reports on NMR Spectroscopy*, ed. G. A. Webb, Academic Press, 2007, vol. 62, pp. 49-114.
8. C. D. Pilgrim, C. A. Colla, G. Ochoa, J. H. Walton and W. H. Casey, *Communications Chemistry*, 2018, **1**, 67.
9. O. C. Compton, B. Jain, D. A. Dikin, A. Abouimrane, K. Amine and S. T. Nguyen, *ACS Nano*, 2011, **5**, 4380-4391.
10. J. Xia, H. Guo, G. Yu, Q. Chen, Y. Liu, Q. Liu, Y. Luo, T. Li and E. Traversa, *Catal. Lett.*, 2021, **151**, 3516-3522.
11. A. Ganguly, S. Sharma, P. Papakonstantinou and J. Hamilton, *The Journal of Physical Chemistry C*, 2011, **115**, 17009-17019.
12. J. Krzystek, A. Ozarowski, J. Telser and D. C. Crans, *Coord. Chem. Rev.*, 2015, **301**, 123-133.

13. J. G. Castle, *Phys. Rev.*, 1953, **92**, 1063-1063.
14. N. C. Halder and C. N. J. Wagner, *Acta Crystallogr.*, 1966, **20**, 312-313.
15. G. Liang, L. Yang, Q. Han, G. Chen, C. Lin, Y. Chen, L. Luo, X. Liu, Y. Li and R. Che, *Advanced Energy Materials*, 2020, **10**, 1904267.
16. C. Liao, Y. Wen, Z. Xia, R. Qin, X. Liu, Y. Yu, B. Shan, T. Zhai and H. Li, *Advanced Energy Materials*, 2018, **8**, 1701621.
17. E. Iwama, N. Kawabata, N. Nishio, K. Kisu, J. Miyamoto, W. Naoi, P. Rozier, P. Simon and K. Naoi, *Acs Nano*, 2016, **10**, 5398-5404.
18. K. Naoi, K. Kisu, E. Iwama, Y. Sato, M. Shinoda, N. Okita and W. Naoi, *J. Electrochem. Soc.*, 2015, **162**, A827-A833.
19. H.-G. Jung, N. Venugopal, B. Scrosati and Y.-K. Sun, *J. Power Sources*, 2013, **221**, 266-271.
20. V. Aravindan, J. Gnanaraj, Y.-S. Lee and S. Madhavi, *Chem. Rev.*, 2014, **114**, 11619-11635.
21. X. N. Xu, F. Niu, D. P. Zhang, C. X. Chu, C. S. Wang, J. Yang and Y. T. Qian, *J. Power Sources*, 2018, **384**, 240-248.
22. L. F. Shen, H. F. Lv, S. Q. Chen, P. Kopold, P. A. van Aken, X. J. Wu, J. Maier and Y. Yu, *Adv. Mater.*, 2017, **29**, 1700142.
23. L. F. Shen, S. Q. Chen, J. Maier and Y. Yu, *Adv. Mater.*, 2017, **29**, 1701571.
24. J. Xu, D. M. Zhang, Z. P. Zhang and S. B. Ni, *Journal of Materials Chemistry A*, 2021, **9**, 10345-10353.
25. N. Okita, E. Iwama and K. Naoi, *Electrochemistry*, 2020, **88**, 83-87.